Understanding the calendering processability of Li(Ni0.33Mn0.33Co0.33)O2-based cathodes

Emiliano Primo, Mehdi Chouchane, Matthieu Touzin, Patricia Vázquez, Alejandro Franco

To cite this version:

Emiliano Primo, Mehdi Chouchane, Matthieu Touzin, Patricia Vázquez, Alejandro Franco. Understanding the calendering processability of Li(Ni0.33Mn0.33Co0.33)O2-based cathodes. Journal of Power Sources, 2021, 488, pp.229361. 10.1016/j.jpowsour.2020.229361 . hal-03114731

HAL Id: hal-03114731
https://hal.science/hal-03114731v1

Submitted on 20 Jan 2021

Contents lists available at ScienceDirect

Journal of Power Sources

journal homepage: www.elsevier.com/locate/jpowsour

Understanding the calendering processability of Li(Ni$_{0.33}$Mn$_{0.33}$Co$_{0.33}$)O$_2$-based cathodes

Emiliano N. Primo [a,b], Mehdi Chouchane [a,b], Matthieu Touzin [c], Patricia Vazquez [d], Alejandro A. Franco [a,b,e,f,*]

[a] Laboratoire de Réactivité et Chimie des Solides (LRCS), UMR CNRS 7314, Université de Picardie Jules Verne, Hub de l'Energie, 15 rue Baudelocque, 80039, Amiens Cedex, France
[b] Réseau sur le Stockage Electrochimique de l'Energie (RS2E), FR CNRS 3459, Hub de l'Energie, 15 rue Baudelocque, 80039, Amiens Cedex, France
[c] Univ. Lille, CNRS, INRAE, Centrale Lille, UMR 8207 - UMET - Unité Matériaux et Transformations, F-59000, Lille, France
[d] GEGENAA EA 3795, University of Reims Champagne – Ardenne, 2, Esplanade Roland Garros, 51100, Reims, France
[e] ALISTORE-European Research Institute, FR CNRS 3104, Hub de l'Energie, 15 rue Baudelocque, 80039, Amiens Cedex, France
[f] Institut Universitaire de France, 103 Boulevard Saint Michel, 75005, Paris, France

HIGHLIGHTS

- The impact of calendering pressure and temperature on NMC cathodes was studied.
- The electrode formulation influences the minimum attainable ε and compressibility.
- Electrochemical performance depends on the morphology of carbon black/binder phase.
- Higher NMC or lower solid content favors film-like CB/binder phase.
- Lower NMC or higher solid content favors agglomerate-like CB/binder phase.

GRAPHICAL ABSTRACT

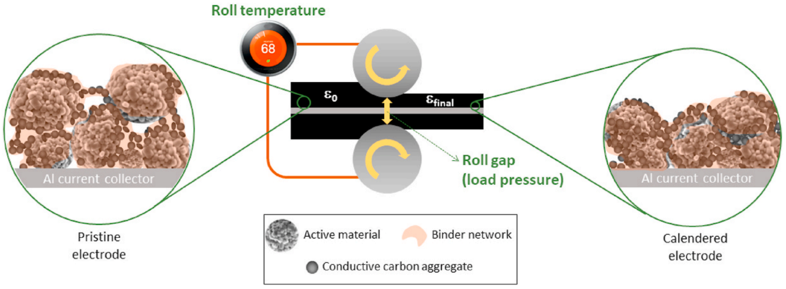

ARTICLE INFO

Keywords:
Lithium ion batteries
NMC Cathodes
Calendering
Mechanical properties
Electrode mesostructure

ABSTRACT

The calendering process aims at enhancing the electrode energy density, and improving the electronic conductivity, and determines the final porous electrode micro/mesostructure. In this sense, one of the main parameters of interest is its impact in the electrode porosity (ε) and the electrochemical performance. Here, we present a systematic study of the calendering conditions (applied calender pressure and roll temperature) effect on the final NMC-based electrodes ε in terms of the active material/carbon additive/binder composition and the amount of solvent used during the preparation of the slurries. The calendering processability was assessed through the cathodes compressibility resistance and minimal attainable ε, the electrode mechanical properties (hardness and elastic deformability), the pore size distribution, the electrode film mesostructure and the C-rate cathode electrochemical performance. Based on our results, it was found that the distribution and organization of the inactive carbon black (CB)/PVdF phase and the electrode mesostructure are the key parameters that control the cathode processability through calendering. Electrodes with high CB/PVdF content and prepared with higher amounts of solvent in the slurry ensure a good electronic conductivity and a film-like structure of the electronic

---

[*] Corresponding author. Laboratoire de Réactivité et Chimie des Solides (LRCS), UMR CNRS 7314, Université de Picardie Jules Verne, Hub de l'Energie, 15 rue Baudelocque, 80039, Amiens Cedex, France.
E-mail address: alejandro.franco@u-picardie.fr (A.A. Franco).

https://doi.org/10.1016/j.jpowsour.2020.229361
Received 8 July 2020; Received in revised form 31 October 2020; Accepted 15 December 2020

conducting phase around the NMC particles which upon calendering outputs a better electrochemical performance.

1. Introduction

The applications of Li-ion batteries (LIB) have sky-rocketed the last three decades due to their unique combination of large capacity, high power and very significant cyclability. A long awaited recognition of the impact of this technology development in industry, society and science in general was achieved when the 2019 Chemistry Nobel Prize was awarded to the original developers of LIB as we know them today [1]. There are still, however, numerous LIB challenges to address, including the need of ever-increasing energy and power densities demands as well as the longevity required in electric vehicle applications. All these can be controlled by knowing the impact of the manufacturing/assembling battery process on the cell performance. The latter includes the slurry preparation and casting, the drying of the solvent, the electrode calendering and the cell assembly conditions [2,3].

Calendering, being at the midpoint in the battery manufacturing process chain, depends on the electrode properties output of the previous manufacturing steps and its output further influences the subsequent steps and the final electrochemical performance of the battery cell [4]. It involves an irreversible mechanical deformation that compacts the particle composite film, increases the extent of the electronic percolation network, enhances the electrode mechanical stability and increases the battery volumetric energy and power densities. An optimal porosity (ε) must be found which maximizes the electrochemical performance, and its value is normally controlled by the inherent electrode properties (such as composition, adherence between the electrode materials and thickness) and the calendering conditions (usually applied load pressure, temperature and line speed) [5]. This is especially true for the positive electrodes, as the common Li-oxide active materials (AM) have low electronic conductivities and are quite sensitive to the conductive carbon network mesostructure [6].

Although the paramount importance of this manufacturing step within the overall process chain, to date few systematic studies have focused on how the calendering impacts the electrode properties/electrochemical performance [7–10]. As an illustration of this, up to date, only few physical models have been developed to provide insights about the calendering, with a limited number of analyzed parameters and compositions. Stershic et al. applied a fabric tensor analysis to discrete element methods (DEM) simulations for modeling the inter-particle contact during the calendering of cathodes [11]. Sangrós-Giménez et al. developed a DEM (parametrized with nanoindentation curves collected on real electrodes) for analyzing the calender pressure impact on graphite and $LiNi_{1\text{-x-y}}Mn_xCo_yO_2$ electrode mesostructures [12–14]. This model treats the electrode as a collection of spheres representing only the AM particles, *i.e.* without an explicit representation of the carbon additive and binder. From a more engineering point of view, Schreiner et al. developed a calender machine/material-process-structure qualitative model to explain correlations between calendering parameters, the machine behavior and electrode structural parameters such as the coating thickness and adhesion strength [15].

In general, the calendering process influences significantly the mechanical and adhesion (to the current collector) properties of the electrodes, the aging of the cell and the final output as to whether the cell will be suited for high-power or high-energy applications. In this sense, Meyer et al. studied the impact of the calendering pressure and roll speed on the compaction resistance, minimal attainable ε and pore size distribution (PSD) on NMC and graphite-based electrodes [8]. Similarly, Schilcher et al. also performed studies on LMO-based cathodes [16]. Additionally, the effect of NMC, NCA, LMO and graphite AM mechanical properties onto the compaction resistance of the resulting electrodes was also analyzed [10]. Also very relevant in terms of electrode processability, Meyer et al. studied how the compaction resistance, adhesion strength and the minimal attainable ε upon calendering are affected upon changing the roll temperature at several calender pressures, in terms of the electrodes mass loadings and their composition [9]. Even though the previous authors made significant contributions into understanding how the calendering process parameters determine the final electrode properties, further understanding is needed to master this key electrode fabrication step.

In this work we analyze the effect of the calendering conditions (applied calender pressure and roll temperature) on the final electrodes' porosities as a function of the AM/carbon additive/binder composition and the amount of solvent used for the preparation of the slurries. Although the effect of electrode film compaction/porosity over some electrode properties/electrochemical output has been studied, this work aims at understanding how those properties can be controlled through the calendering process parameters. A detailed and systematic study of the impact of those formulations parameters was made over the attainable porosities upon calendering, the electrode mechanical properties, the pore size distribution, the electrode mesostructure and the cathodes electrochemical performance. Our study provides a interdependency between the formulation of the electrodes, the impact of the calendering pressure and temperature, the mesostructure of the carbon black/polymer (film-like or agglomerate-like) and the rate capability of the cathodes.

2. Materials and methods

$LiNi_{1/3}Mn_{1/3}Co_{1/3}O_2$ (NMC, average particle diameter = 5 ± 3 μm) was supplied by Umicore. C-NERGY™ super C65 carbon black (CB) was supplied by IMERYS. Solef™ 5130/1001 Polyvinylidene fluoride (PVdF) was purchased from Solvay and N-methylpyrrolidone (NMP) from BASF. All the other reagents were battery grade and were used without further purification.

2.1. Electrodes processing

The slurry solid components NMC, CB and PVdF were premixed with a soft blender. Afterwards, NMP was added until reaching the desired ratio between the solid components and the solvent (slurry's solid content, SC). The mixture was performed in a Dispermat CV3-PLUS high-shear mixer for 2 h in a water-bath cooled recipient at 25 °C. The slurry was coated over a 22 μm thick Aluminum current collector using a comma-coater prototype-grade machine (PDL250, People & Technology, Korea), fixing the gap at 300 μm and the coating speed at 0.3 m min^{-1}. The electrodes were dried in a built-in two-parts oven at 80 and 95 °C. The mass fractions and properties of the electrodes are presented

Table 1

Characteristics of the NMC cathodes used in this work.

Electrode abbreviation	96-2-2-SC-69	95-2.5-2.5-SC-69	94-3-3-SC-69	94-3-3-SC-60
NMC (wt. %)	96	95	94	94
CB (wt. %)	2	2.5	3	3
PVdF (wt. %)	2	2.5	3	3
Solid content (%)	69	69	69	60
Mass loading/mg cm^{-2}	39.5 ± 0.8	36.7 ± 0.6	39 ± 1	28.5 ± 0.3
Initial thickness/μm	180 ± 4	171 ± 3	179 ± 5	149 ± 2
Initial porosity (ε_0)	0.42 ± 0.02	0.475 ± 0.003	0.461 ± .005	0.487 ± 0.005

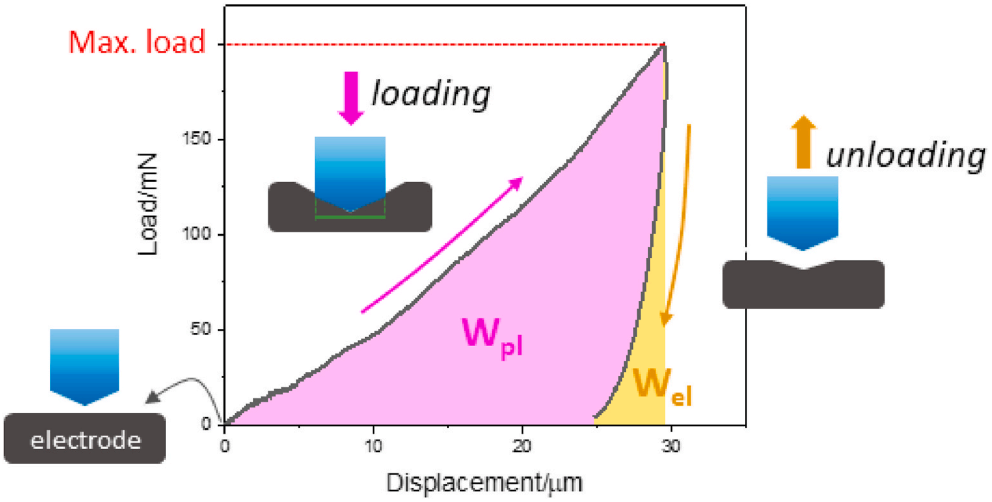

Fig. 1. Load-displacement curve of a microindentation experiment. The magenta-shaded area corresponds to the plastic work (W_{pl}) done by the indenter during the loading, while the yellow-shaded one corresponds to the recovered elastic work (W_{el}) during the indenter unloading. (For interpretation of the references to colour in this figure legend, the reader is referred to the Web version of this article.)

in Table 1. These mass fractions were chosen because of their industrial relevance, as the electrodes here prepared have high AM content.

The electrodes were calendered with a prototype-grade lap press calender (BPN250, People & Technology, Korea). The latter consists in a two-roll compactor of 25 cm of diameter in which the gap between the rolls controls the pressure applied to the electrodes. Furthermore, both the roll speed and the roll temperature can be controlled. The calendering was performed at various applied pressures and at constant line speed (0.54 m min^{-1}) and two different roll temperatures (60 and 75 °C). The dimension of the calendered electrodes were of 10 × 20 cm.

2.2. Electrodes characterization

Porosities were calculated according to

$$\varepsilon = 1 - \frac{m_{el}\left(X_{NMC}/\rho_{NMC} + X_{CB}/\rho_{CB} + X_{PVdF}/\rho_{PVdF}\right)}{V_{el}} \qquad 1$$

where X and ρ are the mass fractions in the electrode and densities of the three solid components NMC/Carbon Black (CB)/PVdF and m_{el} and V_{el} correspond to the electrode mass and volume, respectively. The porosities were measured on 10 different 13 mm diameter disks (punched from different regions of the calendered film electrodes) so the results presented in this work represent an average with n = 10.

The analysis of ε vs. calender pressure profiles is based on the Heckel equation [17] (Eq. (2)), which was adapted to analyze the compressibility of composite electrodes

$$\varepsilon = \varepsilon_{min} + (\varepsilon_0 - \varepsilon_{min}) \exp\left(-P/_{\gamma_C}\right) \qquad 2$$

where ε_0 and ε_{min} are the initial and minimum attainable porosities, respectively, P is the calender applied pressure and γ_C is compaction resistance. Heckel assumed that the ε decrease during powder compaction follows a first order kinetics-like behavior. This expression, largely used in the domains of metallurgy and pharmaceutics, has been recently applied to analyze the calendering of LIB electrodes [9,18].

Microindentation experiments were carried out at room temperature with a microhardness Tester (MHT, CSM Instruments) equipped with a Vickers diamond indenter. The loading/unloading rate was 0.4 mN s^{-1} and the maximum load for all the indentation experiments was of 200 mN, which ensures an indenter penetration lower than 10% of the electrodes thickness, in order to avoid substrate effects. Before unloading, the indenter was maintained at the maximum load during 3 s. Thirty indentation tests were performed for each testing condition to ensure representative results. The electrodes hardness (H) was determined by the Oliver-Pharr method [19]. A scheme of an indentation curve and the main features that can be taken out of it are shown in Fig. 1.

Porosity characterizations were carried out by using a Hg intrusion porosimeter (Micromeritics Autopore IV 9500) reaching a pressure equal to 228 MPa and measuring pore radii sizes from 0.0055 to 360 μm. The results are expressed as open porosity to mercury injection and pore radii access distribution.

The SEM images were acquired with a SEM-FEG Zeiss Crossbeam Neon40 with an Atlas5 module, using a voltage of 10 kV. For statistical purposes, mosaic images were obtained along all the thickness of the electrode, in a portion of the electrode oscillating between 1 and 2.3 mm. The electrodes were polished through ionic cryo-polishing under high vacuum in order to obtain a smooth surface. To that end, a Leica EM TIC 3X Ion Beam Slope Cutter device was used, which has 3 convergent broad beams of Ar^{+} on a static tungsten carbide mask. The image segmentation was performed through the Weka Trainable Segmentation plugin on the ImageJ 1.53c software, using three different phase classes: NMC, carbon binder domain (CBD) and pores. The segmented images were loaded into an *in-house* Matlab code to analyze them in terms of pore and CBD volume fractions along the electrode thickness. For it, the labeled pixels for each phase were normalized by the total amount of pixels of electrode slices of 2 μm. Furthermore, for each CBD cluster the surface and perimeter were calculated and the ratio between them was used to construct surface-to-perimeter ratio histograms.

Electrochemical characterizations were performed in 2032-type coin cells in a half-cell configuration (working electrode area: 1.327 cm^{2}) with a Li foil counter/reference electrode. A 1.0 M $LiPF_6$ solution in ethylene carbonate:dimethyl carbonate (1:1 wt) was used as the electrolyte. The half-cells were assembled in a glovebox (Braun) with a H_2O and O_2 content lower that 0.1 ppm. The galvanostatic charge/discharge experiments were carried out using a BCS-810 series battery cycler (BioLogic, Seyssinet-Pariset, France) in the voltage range of 3.0–4.3 V. The formation cycle was performed by cycling the cell in the same voltage range at C/10. The half-cells were cycled at C/10, C/5, C and 2C and then back to C/10 for 5 charge/discharge cycles each, except for the last C/10 which was done for 10 cycles. 1C corresponds to the current for discharging an NMC electrode in 1 h (specific capacity = 170 mAh g^{-1}). Reported electrochemical results correspond to the average of 3 different independent experiments. All the electrochemical experiments were performed at 25 ± 1 °C.

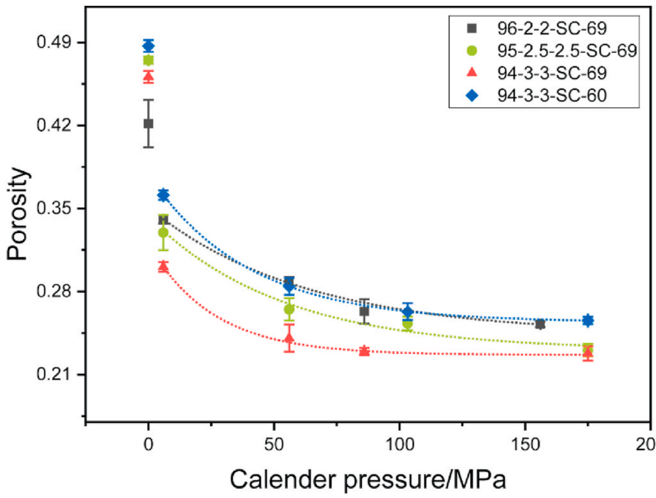

Fig. 2. Porosity evolution of the NMC cathodes 96-2-2-SC-69 (black), 95-2.5-2.5-SC-69 (green), 94-3-3-SC-69 (red) and 94-3-3-SC-60 (blue). The dotted lines represent the fitting of the compaction curves with the Heckel equation (Eq. (2)). Table 2 shows the output of the fitting results. Fig. S2 A (in the Supporting Information) shows the electrodes thickness dependence with the applied pressure. (For interpretation of the references to colour in this figure legend, the reader is referred to the Web version of this article.)

Table 2
Minimal porosity (ε_{min}) and compressibility factor (γ_C), derived from the Heckel equation fitting of the data in Fig. 1.

Electrode	ε_{min}	γ_C/MPa
96-2-2-SC-69	0.243 ± 0.005	62 ± 5
95-2.5-2.5-SC-69	0.230 ± 0.005	53 ± 1
94-3-3-SC-69	0.225 ± 0.008	26 ± 5
94-3-3-SC-60	0.254 ± 0.001	39.5 ± 0.5

3. Results and discussion

Fig. 2 presents the compaction curves (ε vs. calender pressure) for the four different essayed electrodes. Upon calendering the pristine electrodes, there is a steep decrease in ε and then it decreases exponentially to a minimum. As it can be seen in the plot, the fitting with the Heckel equation was not possible considering ε of the uncalendered electrodes (ε_0). This law can be used when the friction between the particles (and/or its plastic/elastic deformation) are the main phenomena that control the compaction process. In this sense, at very low calendering pressures, there is a particles rearrangement due to the collapse of the bigger less mechanically stable pores formed during the electrode drying step. As the calendering pressure increases, the contact area between the NMC and the CB particles surrounded by the PVdF polymer increases therefore favoring friction between the particles. The densification of electrodes can be thus divided in two different regions: a less compact for low pressures (high to intermediate ε) and a densely compacted composite for low ε.

At constant SC, ε_{min} follows the order 96-2-2 > 95-2.5-2.5 > 94-3-3. When comparing constant composition and decreasing the amount of solids within the slurry used to prepare the electrodes (94-3-3-SC 69 vs. 60), ε_{min} further increases. This means that the higher the amount of solvent used to prepare the slurry, the higher the minimal attainable porosity through calendering.

The friction between the NMC and CB particles and its relation with the total surface area of contact were acknowledged to be among the most important characteristics that determine the pressure needed to densify or compact the electrodes [10]. This resistance can be quantified by the γ_C parameter extracted from the fitting of Eq. (2). At constant SC, γ_C decreases from 96-2-2 to 94-3-3. In the latter composition, when reducing the SC, γ_C increases.

In order to understand the previous results, the mechanical properties of the electrodes were measured by means of microindentation. Fig. 3 A presents the hardness (H) for the 4 different electrodes as a function of the ε and the calender applied pressure (inset). H is related to the material resistance to plastic deformation and it is an essential factor that determines the processability during calendering [20]. Although there are many microstructural factors that affect H, ε is a critical one, as by reducing it, it exponentially increases H [21]. While H values for all the electrodes in all the conditions span up to 150 MPa, the reported H values for NMC and the CB/PVdF matrix are 11.2 GPa [22] – 8.89 GPa [23] and 130–40 MPa [23], respectively. Taking into account that the projected areas of contact between the indenter and the electrode (at maximal load) range between $10^3 - 2 \times 10^4$ μm^2 and that the average NMC particle diameter is 5 ± 3 μm, the observed H values are mainly determined by the CB/PVdF matrix surrounding the NMC particles. This is very important, as it demonstrates that the mechanical properties of the less voluminous phase ($\varphi_{CB/PVdF} = 0.097$, 0.119 and 0.141 for 96-2-2, 95-2.5-2.5 and 94-3-3, respectively) are the ones that determine the final properties of the electrodes.

At constant SC, increasing the amount of CB/PVdF produces an increase in H when comparing the same values of ε. Furthermore, when comparing electrodes at constant composition and decreasing SC, H decreases. In this sense, harder electrodes are the ones that have higher amount of CB/PVdF or the ones that were prepared with lower amounts of solvent (during the slurry preparation). These harder electrodes are associated with conditions in which lower porosities are attained through calendering.

Panel B of Fig. 3 shows the ratio between the elastic (W_{el}) and the plastic work (W_{pl}) as a function of ε and the calender applied pressure (inset). Both works were calculated by integrating the areas under the microindentation curve during the indenter loading and unloading, respectively (Fig. 1). While W_{pl} represents the irreversible deformation produced upon indentation, W_{el} represents the ability of the indented substrate to return to its initial shape [24]. As we formerly discussed, the indentation work comes mainly from the CB/PVdF network within the electrode. It is formed by nano/micro aggregates of CB particles surrounded by the PVdF polymer, establishing a visco-elastic solid matrix. Being a solid particle, it is expected that CB H and Young modulus will be high, while for PVdF H is 59 ± 3 MPa (Fig. S4, in the Supporting Information). In this sense, W_{el}/W_{pl} gives information about the strength and number of binding sites between the CB particles due to the presence of the PVdF [9,16].

The W_{el}/W_{pl} values are quite low for most of the compositions and ε, which means that the deformation induced by the indenter is mainly irreversible. This is not surprising, as by checking the representative load-displacement curves of Fig. S1, it can be seen that there is almost no recovery in the unloading part. In general terms, W_{el}/W_{pl} values have the following order: 94-3-3-SC-69 < 95-2.5-2.5-SC-69 $\gtrsim$ 96-2-2-SC-69 < 94-3-3-SC-60. Interestingly, it emulates exactly the same trend as the γ_C (Table 2). This means that the electrodes compressibility is related to the number of contacts between the particles and the extent of binding by the PVdF. Indeed, increasing the amount of CB/PVdF outputs a more cross-linked network [25] causing more friction between the particles. Nonetheless, following the previous logic it would be expected that at SC = 69, the resistance to compaction (or W_{el}/W_{pl}) of 94-3-3 would be the highest and this is not the case for low porosities, while when the electrode is calendared close to ε_{min} values W_{el}/W_{pl} increases steeply. A careful inspection of both H and W_{el}/W_{pl} shows that, at high ε values, the irreproducibility of the measurements (note the size of the standard deviation bars) is quite high. This would imply the presence of heterogeneous distribution of the solid particles and the PVdF within the electrode microstructure and it will be discussed briefly. On the other hand, the fact that increasing the amount of solvent used for the preparation of the slurry makes more difficult the compressibility of the

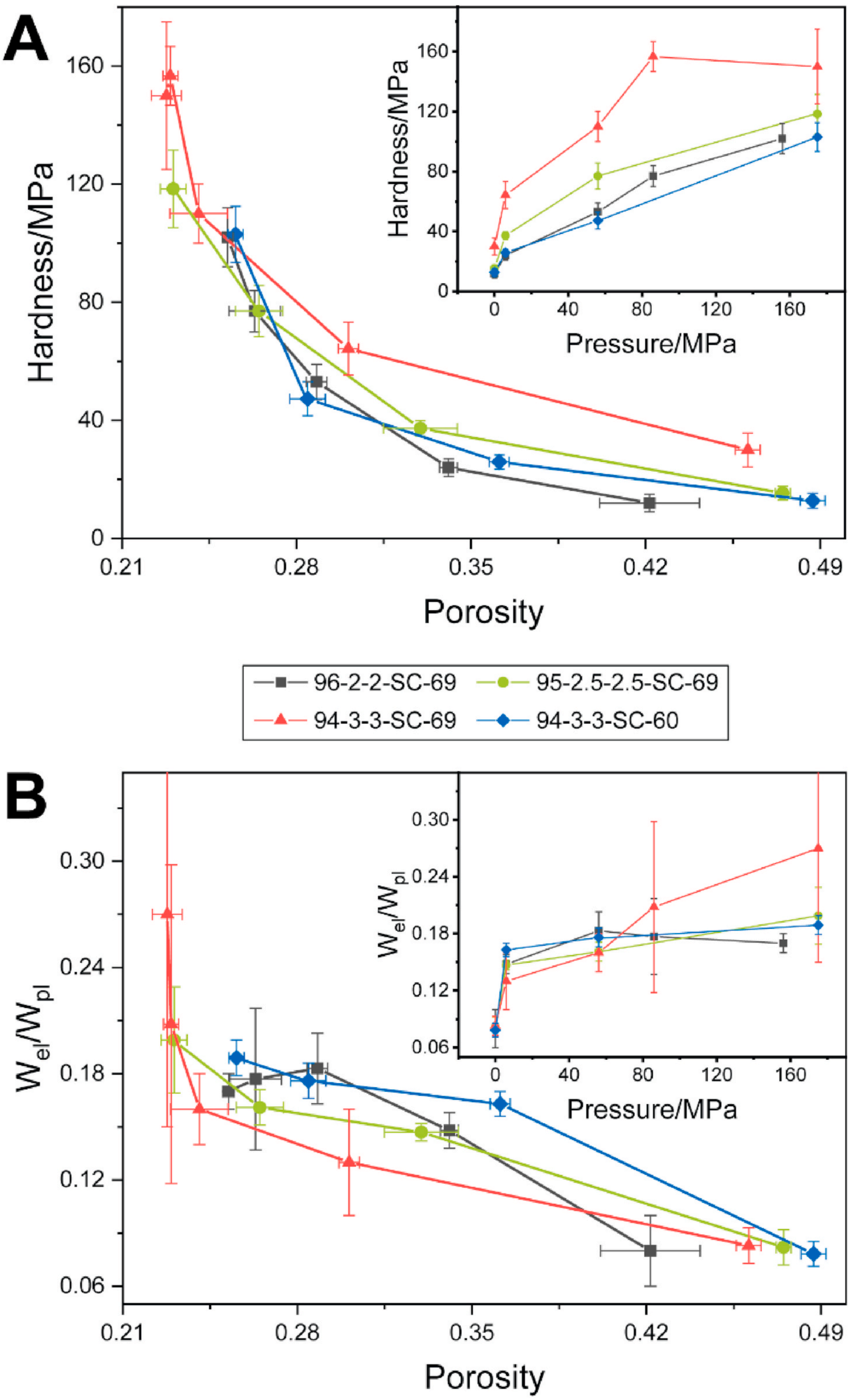

Fig. 3. Average hardness (A) and elastic-to-plastic work ratio (B) in terms of the electrodes porosity and the calender applied pressure (insets). The bars correspond to the standard deviation of 30 microindentation measurements at each condition. The representative load-displacement microindentation curves are reported in Fig. S1, in the Supporting Information.

electrode is related to its more elastic behavior upon calendering. In a previous work [26], we demonstrated that in high PVdF-content slurries the addition of NMP solvent induces a solid-like behavior that outputs higher ε after the drying process. This solid-like elastic behavior makes calendering more difficult as it relies in an irreversible deformation of the electrode structure.

The incremental (A) and cumulative (B) pore size distribution (PSD) for the different non calendered (full lines) and calendered (dotted lines) cathodes are shown in Fig. 4. Two different pore radii access regions can be found in it: the region I (lower than ~ 0.1 μm) and the region II, which corresponds to values between 0.1 and 2 μm [27,28]. For the non calendered electrodes, the region II pore radius is independent of the

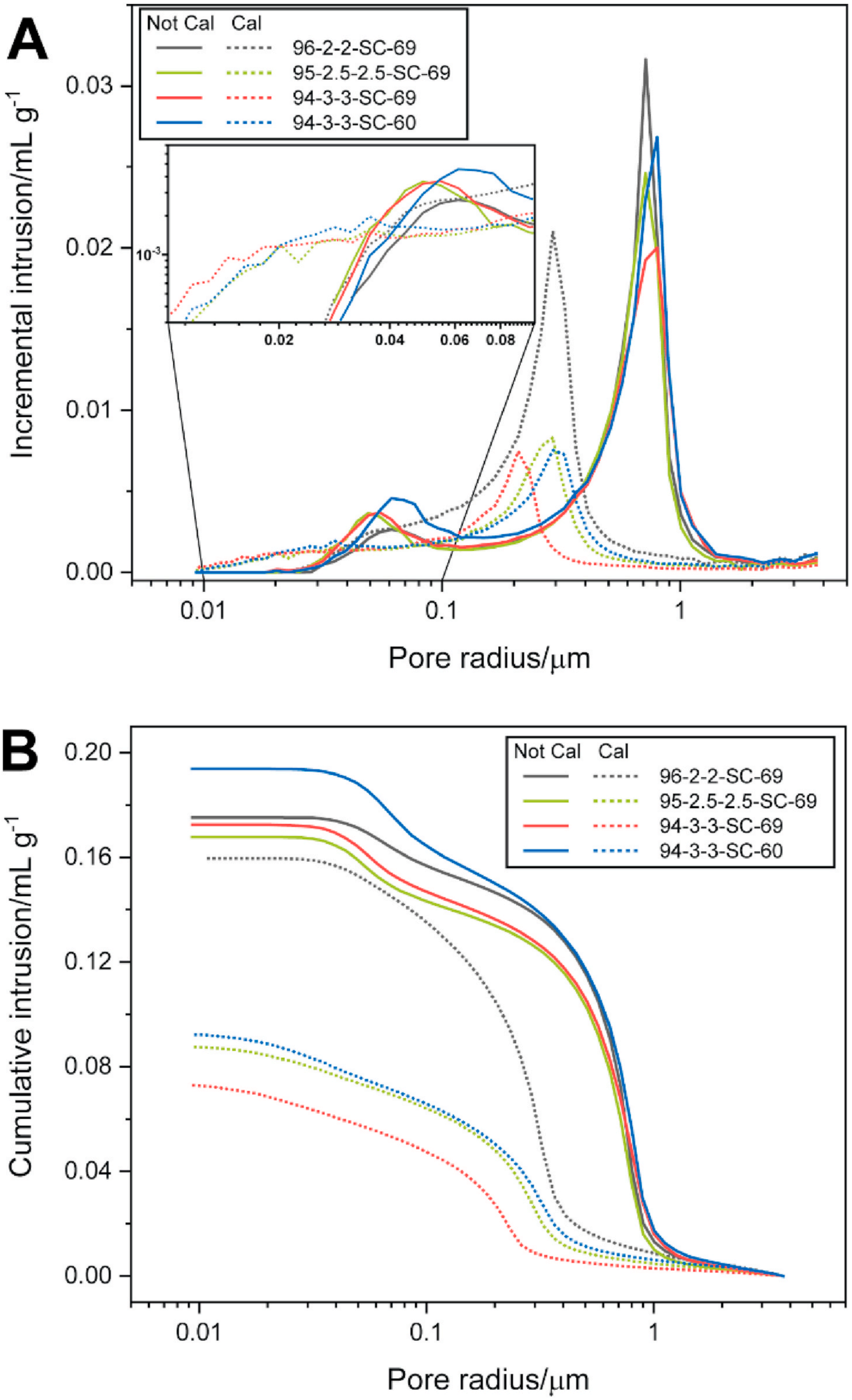

Fig. 4. Incremental (A) and cumulative (B) pore size distribution for the non-calendared (full lines) and calendared (dotted lines, applied pressure = 90 MPa) electrodes. The inset in panel A corresponds to the PSD between 0.01 and 0.1 µm, in log-log scale.

composition and the SC, while their absolute volumes decrease, in terms of the AM content, as 96-2-2-SC-69 > 95-2.5-2.5-SC-69 > 94-3-3-SC-69; and in terms of the SC, as 94-3-3-SC-60 > 94-3-3-SC-69. The region I pore radii are the highest for 96-2-2-SC-69 and 94-3-3-SC-60, while their volume increases when reducing the AM mass fraction and the SC. The above points out that by increasing the AM mass fraction or reducing the SC, the proportion of region II pores increases, while the opposite favors the smaller region I pores.

Upon calendering (dotted lines in the Fig. 4), both the region II pore radius and volume are drastically reduced for 95-2.5-2.5-SC-69 and 94-3-3-SC-69 cathodes, while their region I pores represent more than half of the total porosity. In the case of 96-2-2-SC-69, although lower, the region II pores still represent the main contribution to the overall electrode ε. When reducing the SC in the 94-3-3 cathodes, the region II mean pore radius and volume are higher while the region I pores have a higher contribution from higher radii. Furthermore, a careful inspection in this region shows that lower pore radii can be attained when reducing the AM amount and the SC (inset in Fig. 4 A).

Fig. 5 shows the electrodes cross-section SEM images for the four different compositions, calendered at 90 MPa and 60 °C. The NMC and CBD phases can be easily distinguished within the electrodes: when comparing constant SC and reducing the amount of AM, the CBD phase has a more extended distribution along the electrode. In order to understand the influence of the AM/CB relative amount and the SC on the electrodes microstructure organization, the SEM images were segmented into 3 phases (namely AM, CBD and pores) and then the resulting data was analyzed. The segmentation analysis, presented in Fig. 6 A and B, shows the porosity and CBD volume fraction (φ_{CBD}) profiles, respectively, along the electrode thickness (vertical direction in the SEM images of Fig. 5). For the 96-2-2-SC-69 electrode there is an inhomogeneous distribution of the porosity, while increasing the amount of CB and binder outputs a less fluctuating profile. However, for the case of 94-3-3-SC-69 there is a clear distribution in the electrode compactness: in the region close to the surface the porosity is low while when approaching to the current collector the compactness of the solid

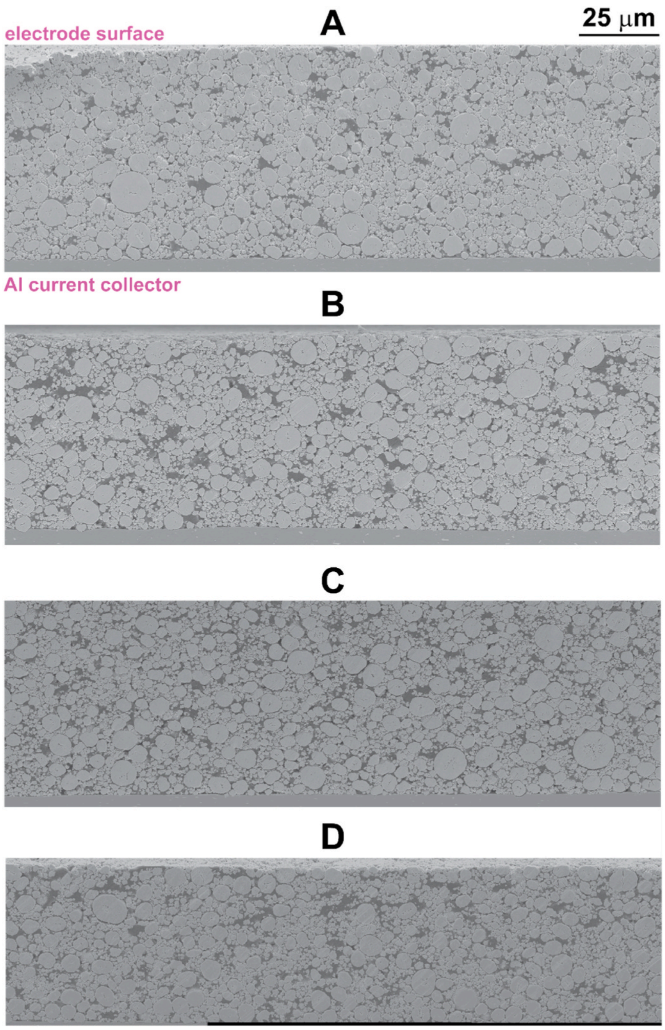

Fig. 5. Electrode cross-section SEM images of 96-2-2-SC-69 (A), 95-2.5-2.5-SC-69 (B), 94-3-3-SC-69 (C) and 94-3-3-SC-60 (D). The electrodes were calendered at a pressure equal to 90 MPa and the roll temperature was set to 60 °C. The upper part of each image corresponds to the electrode surface, while at the bottom there is the current collector. The scale is common to all images and is displayed in the top right of the image.

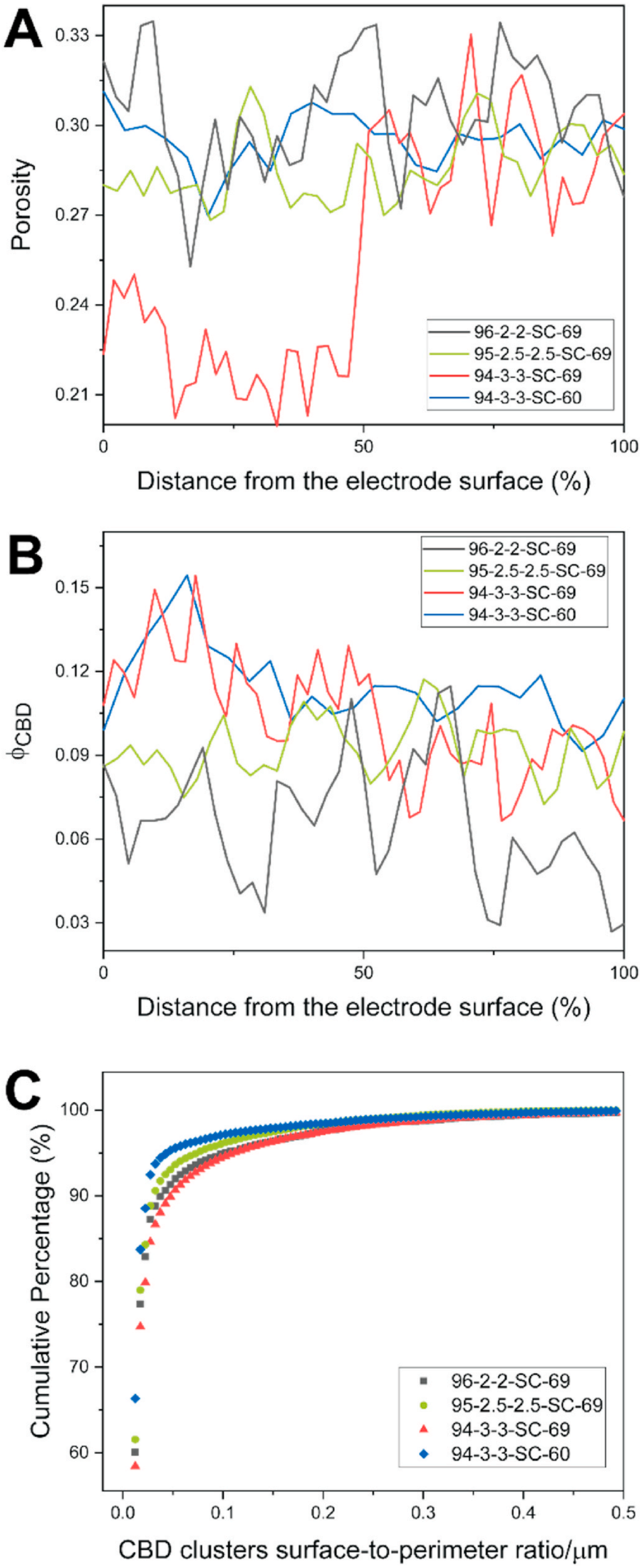

Fig. 6. Cross-section pore (A) and CBD (B) volume fraction profiles along the vertical direction of the segmented SEM images in Fig. 5. Each point was obtained by dividing the electrode into 2 μm height slices. (C) CBD clusters surface-to-perimeter ratio histogram (expressed as a cumulative percentage) for the electrodes.

components is looser. The latter explains the high variability in the mechanical properties (H and W_{el}/W_{pl}) of this electrode. At constant electrode composition, when increasing the amount of solvent there is a more homogeneous distribution of the porosity.

The φ_{CBD} gives further information about the electrode meso-structure. At constant SC, and just as the porosity distribution, when comparing 96-2-2 vs. 95-2.5-2.5 there is a more homogeneous distribution of the CBD phase along the electrode thickness for the latter. In the same way, the 94-3-3-SC-69 electrode has an uneven distribution along the thickness: there is a higher amount of CBD in the regions next to the electrode surface and its volume fraction tends to decrease in the regions close to the current collector. When comparing constant composition (94-3-3), the electrode with lower SC has a more homogeneous CBD distribution. In terms of the CBD morphology, Fig. 6 C shows the histograms (presented in terms of cumulative percentage) of the ratio between the CBD cluster surface and its perimeter (for all the clusters of the electrodes cross-sections). It can be easily demonstrated that for 2 shapes with the same area, the perimeter will be higher for the one that has a more extended shape (and therefore it will have a smaller surface to perimeter ratio). In the case of the CBD phase, a lower ratio implies a more extended film-like [29,30] organization of such phase. On the contrary, higher values are associated to a more compact agglomerate-like form [31]. For the 94-3-3-SC-69 electrode, there is a higher contribution of the smaller surface-to-perimeter ratio CBD clusters. In this case, a more extended arrangement of the CBD phase within the AM particles exposes a higher amount of surface area and therefore outputs a higher contribution of the more film-like CBD clusters. On the contrary, the distribution of surface-to-perimeter ratios of 94-3-3-SC-69 electrode is shifted to higher values, indicating a lower extension of the CBD clusters or a more agglomerate-like form. 96-2-2-SC-69 and 95-2.5-2.5-SC-69 electrodes present a contribution within the other two.

The morphology of CB/PVdF phase has a huge impact in the electrochemical performance of the electrodes. Fig. 7 shows the discharge capacities at various C-rates for the electrodes calendered at 90 MPa and 60 °C. At C/10 and C/5, the specific capacities are quite similar which is expectable as at low C-rates the performance is dictated by thermodynamic factors (AM nature and mass) [32]. Upon increasing the current to C, the specific capacities follow the order 94-3-3-SC-60 > 95-2.5-2.5-SC-69–96-2-2-SC-69 > 94-3-3-SC-69. The better performance of 94-3-3-SC-60 (even at 2C) is related to the higher amount of conductive carbon additive and its film-like morphology, which ensures good coverage around the AM particles. This is clear when comparing to the 94-3-3-SC-69 electrode: although it has the same amount of CB/PVdF, its agglomerate-like morphology does not cover in a homogeneous way the NMC particles, reducing its interconnectivity and therefore the electrochemical performance. Furthermore, as seen in Fig. 6 A, the uneven distribution of porosity along the electrode thickness, with the lower one located near the electrode surface, contributes to its poor specific capacity at high C-rate regime.

The analysis of the temperature effect on the calendering process is shown on Fig. 8 A, B and C; where ε, H and W_{el}/W_{pl} (respectively) are depicted in terms of the electrode composition and SC for two different roll temperatures: 60 and 75 °C. In all the cases increasing the roll temperature outputs lower ε. As it is well known, PVdF increases its deformability at higher temperatures due to its thermoplasticity [33]. Therefore, by increasing the temperature, the PVdF network can be more easily deformated, allowing better compaction of the electrodes and therefore achieving lower ε at the same calender pressure. Interestingly, the reduction in the achievable calendered ε is more noticeable for the low AM content cathodes. This is correlated to the fact that these electrodes are ones that experience a higher increase in its H upon calendering (Fig. 8 B).

W_{el}/W_{pl} values (panel C of Fig. 8) show a decrease in 96-2-2-SC-69 and 94-3-3-SC-60, while for 95-2.5-2.5-SC-69 and 94-3-3-SC-69

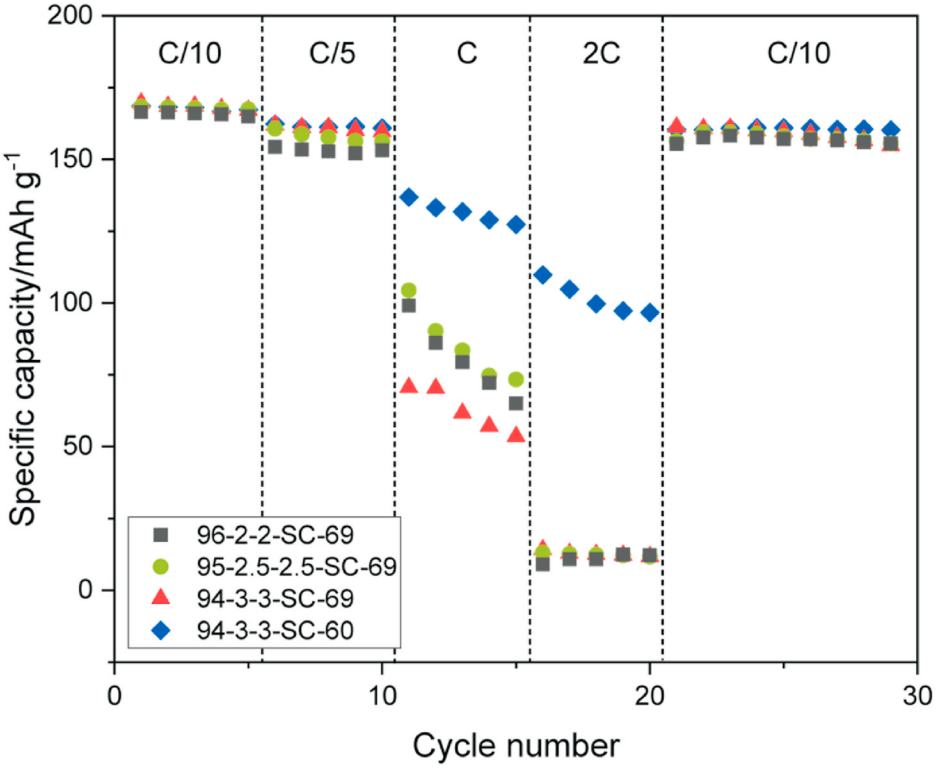

Fig. 7. Rate capability tests for the calendered electrodes (60 °C, 90 MPa) at C/10, C/5, C, 2C and back to C/10. 96-2-2-SC-69 (black square): ε = 0.26 ± 0.01; 95-2.5-2.5-SC-69 (green circle): ε = 0.253 ± 0.006; 94-3-3-SC-69 (red triangle): ε = 0.229 ± 0.003; 94-3-3-SC-60 (blue diamond): ε = 0.263 ± 0.007. The representative charge-discharge curves at C/10 and C rates for each electrode can be found in the Supporting Information, Fig. S5. (For interpretation of the references to colour in this figure legend, the reader is referred to the Web version of this article.)

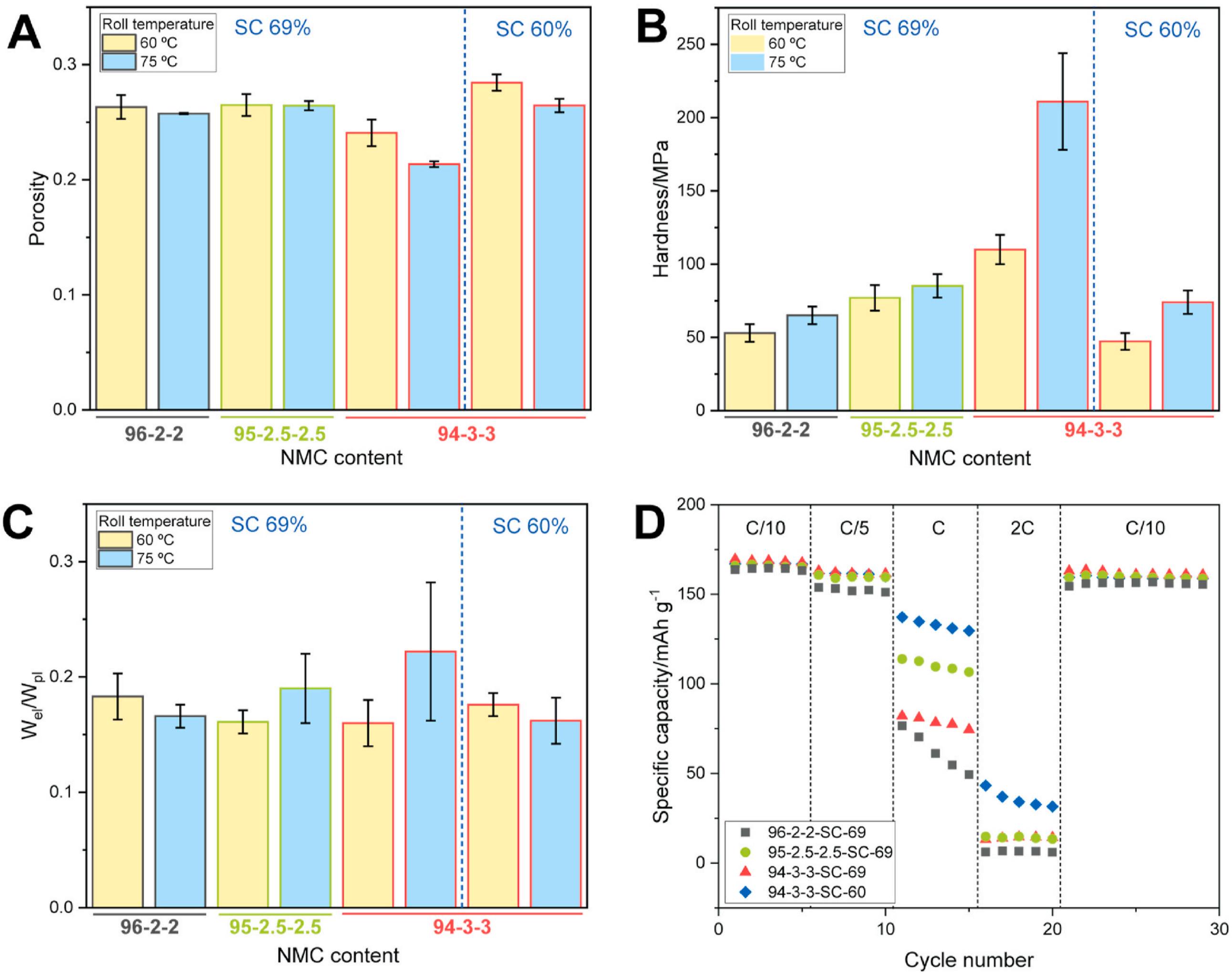

Fig. 8. Average porosity (A), hardness (B) and elastic-to-plastic work ratio (C) in terms of the roll temperature (yellow bars: 60 °C, light blue bars: 75 °C) for electrodes calendered to a pressure of 56 MPa. The values within the bars correspond to the average electrode porosities. (D) Rate capability tests for the calendered electrodes (75 °C, 56 MPa) at C/10, C/5, C, 2C and back to C/10. 96-2-2-SC-69 (black square): $\varepsilon = 0.27 \pm 0.01$; 95-2.5-2.5-SC-69 (green circle): $\varepsilon = 0.258 \pm 0.006$; 94-3-3-SC-69 (red triangle): $\varepsilon = 0.213 \pm 0.002$; 94-3-3-SC-60 (blue diamond): $\varepsilon = 0.264 \pm 0.006$. Fig. S2 B (in the Supporting Information) shows the electrodes thickness dependence with the roll temperature. (For interpretation of the references to colour in this figure legend, the reader is referred to the Web version of this article.)

display an increase. Being the PVdF a thermoplastic polymer, the increase in the temperature will reduce the friction between the particles and favor particles rearrangement to a more compact way. Therefore, for the electrodes with CB/PVdF film-like structure (96-2-2-SC-69 and 94-3-3-SC-60), the increase in the temperature will favor the densification of that phase. On the contrary, for the electrodes with agglomerate-like inactive phase distribution (95-2.5-2.5-SC-69 and 94-3-3-SC-69) it will benefit a more spread distribution of it. This is reflected in the electrochemical performance of the cathodes at high C-rate (Fig. 8D), where the specific capacities at 2C of the 94-3-3-SC-60 fells around 63%, while the specific capacities of 95-2.5-2.5-SC-69 and 94-3-3-SC-69 at C increase 32 and 43%, respectively, compared to the performances of the calendared electrodes at 60 °C. As it can be seen, increasing the calendering temperature does not change the intrinsic features of the electrodes but rather tunes the behavior at high C-rates.

4. Conclusions

In this paper we analyzed the calendering processability of NMC-based cathodes in terms of the formulation parameters, such as the relative amount between the AM and the inactive phases (CB and PVdF) and the amount of solvent. Their impact based on the applied pressure and the roll temperature was studied through the minimal attainable electrode porosities, the mechanical properties, the pore size distribution and the electrode mesostructure. The electrodes with the lowest porosities were the ones with high SC and low amount of AM. This is so because of the organization of the CB/PVdF polymer phase around the active material particles. Lower porosities are favored when that phase is organized in an agglomerate-like manner, as the void space between the bigger active material particles is more efficiently occupied. On the contrary, when the amount of AM is high or for electrodes prepared with a high amount of solvent during the slurry formulation, the CB/PVdF polymer phase forms a film-like structure that output higher porosities, even after calendering. In terms of the cathodes rate capabilities, the higher electrochemical performances are reached for film-like structures with high CB/PVdF content. Upon increasing the temperature, the thermoplasticity of the PVdF favors the flow of the CB/PVdF phase. These features prove that the final electrode properties are a function of the interdependencies between the different manufacturing steps. Furthermore, this work represents a step further into bringing new insights for an accurate control of the electrode mesostructure which impacts the electrochemical performance of the final batteries. Finally, we believe that the produced data and unraveled interdependencies are also very useful in the development of predictive machine learning and physical models as we are demonstrating elsewhere in our ARTISTIC project [34-36].

CRediT authorship contribution statement

Emiliano N. Primo: Conceptualization, Methodology, Formal analysis, Data curation, Investigation, Visualization, Writing - review & editing, Writing - original draft. **Mehdi Chouchane:** Software, Methodology, Formal analysis, Software, Visualization, Writing - review & editing. **Matthieu Touzin:** Investigation, Validation, Resources, Writing - review & editing. **Patricia Vazquez:** Investigation, Validation, Resources, Writing - review & editing. **Alejandro A. Franco:** Conceptualization, Methodology, Writing - review & editing, Supervision, Project administration, Funding acquisition.

Declaration of competing interest

The authors declare that they have no known competing financial interests or personal relationships that could have appeared to influence the work reported in this paper.

Acknowledgements

A.A.F., M.C. and E.P. acknowledge the European Union's Horizon 2020 research and innovation programme for the funding support through the European Research Council (grant agreement 772873, "ARTISTIC" project). A.A.F. acknowledges Institut Universitaire de France for the support. We thankfully acknowledge Imène Esteve and the Institut de Minéralogie, de Physique des Matériaux et de Cosmochimie (IMPMC, UMR 7590) facilities, in which the ionic polishing/SEM experiments were performed: they are supported by Région Île-de-France Grant SESAME 2006 NOI-07-593/R, INSU-CNRS, INP-CNRS, UPMC and by the French National Research Agency (ANR) Grant ANR-07-BLAN-0124-01.

Appendix B. Supplementary data

Supplementary data to this article can be found online at https://doi.org/10.1016/j.jpowsour.2020.229361.

References

[1] D. Castelvecchi, E. Stoye, Chemistry Nobel honours world-changing batteries, Nature 574 (2019), https://doi.org/10.1038/d41586-019-02965-y, 308–308.
[2] S. Dühnen, J. Betz, M. Kolek, R. Schmuch, M. Winter, T. Placke, Toward green battery cells: perspective on materials and technologies, Small Methods (2020) 2000039, https://doi.org/10.1002/smtd.202000039, n/a.
[3] W.B. Hawley, J. Li, Electrode manufacturing for lithium-ion batteries—analysis of current and next generation processing, J. Energy Storage. 25 (2019) 100862, https://doi.org/10.1016/j.est.2019.100862.
[4] M. Thomitzek, O. Schmidt, F. Röder, U. Krewer, C. Herrmann, S. Thiede, Simulating process-product interdependencies in battery production systems, Procedia CIRP 72 (2018) 346–351, https://doi.org/10.1016/j.procir.2018.03.056.
[5] V. Laue, F. Röder, U. Krewer, Joint structural and electrochemical modeling: impact of porosity on lithium-ion battery performance, Electrochim. Acta 314 (2019) 20–31, https://doi.org/10.1016/j.electacta.2019.05.005.
[6] Y.H. Chen, C.W. Wang, X. Zhang, A.M. Sastry, Porous cathode optimization for lithium cells: ionic and electronic conductivity, capacity, and selection of materials, J. Power Sources 195 (2010) 2851–2862, https://doi.org/10.1016/j.jpowsour.2009.11.044.
[7] O. Schmidt, M. Thomitzek, F. Röder, S. Thiede, C. Herrmann, U. Krewer, Modeling the impact of manufacturing uncertainties on lithium-ion batteries, J. Electrochem. Soc. 167 (2020), 060501, https://doi.org/10.1149/1945-7111/ab798a.
[8] C. Meyer, H. Bockholt, W. Haselrieder, A. Kwade, Characterization of the calendering process for compaction of electrodes for lithium-ion batteries, J. Mater. Process. Technol. 249 (2017) 172–178, https://doi.org/10.1016/j.jmatprotec.2017.05.031.
[9] C. Meyer, M. Weyhe, W. Haselrieder, A. Kwade, Heated calendering of cathodes for lithium-ion batteries with varied carbon black and binder contents, Energy Technol. 8 (2020) 1900175, https://doi.org/10.1002/ente.201900175.
[10] C. Meyer, M. Kosfeld, W. Haselrieder, A. Kwade, Process modeling of the electrode calendering of lithium-ion batteries regarding variation of cathode active materials and mass loadings, J. Energy Storage. 18 (2018) 371–379, https://doi.org/10.1016/j.est.2018.05.018.
[11] A.J. Stershic, S. Simunovic, J. Nanda, Modeling the evolution of lithium-ion particle contact distributions using a fabric tensor approach, J. Power Sources 297 (2015) 540–550, https://doi.org/10.1016/j.jpowsour.2015.07.088.
[12] C. Sangrós Giménez, B. Finke, C. Nowak, C. Schilde, A. Kwade, Structural and mechanical characterization of lithium-ion battery electrodes via DEM simulations, Adv. Powder Technol. 29 (2018) 2312–2321, https://doi.org/10.1016/j.apt.2018.05.014.
[13] C. Sangrós Giménez, B. Finke, C. Schilde, L. Froböse, A. Kwade, Numerical simulation of the behavior of lithium-ion battery electrodes during the calendaring process via the discrete element method, Powder Technol. 349 (2019) 1–11, https://doi.org/10.1016/j.powtec.2019.03.020.
[14] C. Sangrós Giménez, C. Schilde, L. Froböse, S. Ivanov, A. Kwade, Mechanical, electrical, and ionic behavior of lithium-ion battery electrodes via discrete element method simulations, Energy Technol. 8 (2020) 1900180, https://doi.org/10.1002/ente.201900180.
[15] D. Schreiner, M. Oguntke, T. Günther, G. Reinhart, Modelling of the calendering process of NMC-622 cathodes in battery production analyzing machine/material–process–structure correlations, Energy Technol. 7 (2019) 1900840, https://doi.org/10.1002/ente.201900840.
[16] C. Schilcher, C. Meyer, A. Kwade, Structural and electrochemical properties of calendered lithium manganese oxide cathodes, Energy Technol. 4 (2016) 1604–1610, https://doi.org/10.1002/ente.201600130.
[17] R.W. Heckel, Density-pressure relationships in powder compaction, Trans. Metall. Soc. AIME. 221 (1961) 671–675.
[18] J.K. Mayer, L. Almar, E. Asylbekov, W. Haselrieder, A. Kwade, A. Weber, H. Nirschl, Influence of the carbon black dispersing process on the microstructure and performance of Li-ion battery cathodes, Energy Technol. 8 (2020) 1900161, https://doi.org/10.1002/ente.201900161.
[19] W.C. Oliver, G.M. Pharr, An improved technique for determining hardness and elastic modulus using load and displacement sensing indentation experiments, J. Mater. Res. 7 (1992) 1564–1583, https://doi.org/10.1557/JMR.1992.1564.
[20] R. Rice, Mechanical Properties of Ceramics and Composites, first ed., CRC Press, Boca Raton, 2000 https://doi.org/10.1201/9780203908471.
[21] Y. Wang, Q. Zhang, D. Li, J. Hu, J. Xu, D. Dang, X. Xiao, Y.-T. Cheng, Mechanical property evolution of silicon composite electrodes studied by environmental nanoindentation, Adv. Energy Mater. 8 (2018) 1702578, https://doi.org/10.1002/aenm.201702578.
[22] E.J. Cheng, K. Hong, N.J. Taylor, H. Choe, J. Wolfenstine, J. Sakamoto, Mechanical and physical properties of LiNi0.33Mn0.33Co0.33O2 (NMC), J. Eur. Ceram. Soc. 37 (2017) 3213–3217, https://doi.org/10.1016/j.jeurceramsoc.2017.03.048.
[23] L.S. de Vasconcelos, R. Xu, J. Li, K. Zhao, Grid indentation analysis of mechanical properties of composite electrodes in Li-ion batteries, Extrem. Mech. Lett. 9 (2016) 495–502, https://doi.org/10.1016/j.eml.2016.03.002.
[24] Y.-T. Cheng, C.-M. Cheng, Scaling, dimensional analysis, and indentation measurements, Mater. Sci. Eng. R Rep. 44 (2004) 91–149, https://doi.org/10.1016/j.mser.2004.05.001.
[25] J. Chen, J. Liu, Y. Qi, T. Sun, X. Li, Unveiling the roles of binder in the mechanical integrity of electrodes for lithium-ion batteries, J. Electrochem. Soc. 160 (2013), https://doi.org/10.1149/2.088309jes. A1502–A1509.
[26] R.P. Cunha, T. Lombardo, E.N. Primo, A.A. Franco, Artificial intelligence investigation of NMC cathode manufacturing parameters interdependencies, Batter. Supercaps. 3 (2020) 60–67, https://doi.org/10.1002/batt.201900135.
[27] M. Haarmann, W. Haselrieder, A. Kwade, Extrusion-based processing of cathodes: influence of solid content on suspension and electrode properties, Energy Technol. 8 (2020) 1801169, https://doi.org/10.1002/ente.201801169.
[28] N. Besnard, A. Etiemble, T. Douillard, O. Dubrunfaut, P. Tran-Van, L. Gautier, S. Franger, J.-C. Badot, E. Maire, B. Lestriez, Multiscale morphological and electrical characterization of charge transport limitations to the power performance of positive electrode blends for lithium-ion batteries, Adv. Energy Mater. 7 (2017) 1602239, https://doi.org/10.1002/aenm.201602239.
[29] H. Bockholt, W. Haselrieder, A. Kwade, Intensive powder mixing for dry dispersing of carbon black and its relevance for lithium-ion battery cathodes, Powder Technol. 297 (2016) 266–274, https://doi.org/10.1016/j.powtec.2016.04.011.

[30] W. Bauer, D. Nötzel, V. Wenzel, H. Nirschl, Influence of dry mixing and distribution of conductive additives in cathodes for lithium ion batteries, J. Power Sources 288 (2015) 359–367, https://doi.org/10.1016/j.jpowsour.2015.04.081.

[31] S. Hein, T. Danner, D. Westhoff, B. Prifling, R. Scurtu, L. Kremer, A. Hoffmann, A. Hilger, M. Osenberg, I. Manke, M. Wohlfahrt-Mehrens, V. Schmidt, A. Latz, Influence of conductive additives and binder on the impedance of lithium-ion battery electrodes: effect of morphology, J. Electrochem. Soc. 167 (2020), 013546, https://doi.org/10.1149/1945-7111/ab6b1d.

[32] A. Rucci, A.C. Ngandjong, E.N. Primo, M. Maiza, A.A. Franco, Tracking variabilities in the simulation of Lithium Ion Battery electrode fabrication and its impact on electrochemical performance, Electrochim. Acta 312 (2019) 168–178, https://doi.org/10.1016/j.electacta.2019.04.110.

[33] H. Chen, M. Ling, L. Hencz, H.Y. Ling, G. Li, Z. Lin, G. Liu, S. Zhang, Exploring chemical, mechanical, and electrical functionalities of binders for advanced energy-storage devices, Chem. Rev. 118 (2018) 8936–8982, https://doi.org/10.1021/acs.chemrev.8b00241.

[34] (n.d.), https://www.u-picardie.fr/erc-artistic/.

[35] M. Duquesnoy, T. Lombardo, M. Chouchane, E. Primo, A.A. Franco, Data-driven assessment of electrode calendering process by combining experimental results, in silico mesostructures generation and machine learning, J. Power Sources 480 (2020), 229103, https://doi.org/10.1016/j.jpowsour.2020.229103.

[36] A. Ngandjong, T. Lombardo, E. Primo, M. Chouchane, A. Shodiev, O. Orcelus, A. A. Franco, Investigating electrode calendering and its impact on electrochemical performance by means of a new discrete element method model: Towards a digital twin of Li-Ion battery manufacturing, J. Power Sources 485 (2020), 229320, https://doi.org/10.1016/j.jpowsour.2020.229320.